Fabrication of two-dimensional hard X-ray diffraction gratings

S. Rutishauser[a], M. Bednarzik[a], I. Zanette[b,c], T. Weitkamp[b,d], M. Börner[e], J. Mohr[e], C. David[a]

[a]*Paul Scherrer Institut, 5232 Villigen PSI, Switzerland*
[b]*European Synchrotron Radiation Facility, 38043 Grenoble, France*
[c]*Physics Department, Technische Universität München, Garching, Germany*
[d]*Synchrotron Soleil, 91192 Gif-sur-Yvette, France*
[e]*Karlsruhe Institute of Technology, 76131 Karlsruhe, Germany*

Abstract

Hard X-ray grating interferometry has shown promising results in phase and scattering imaging, as well as in metrology applications. Recently, the technique has been extended to two dimensions, recording the full phase gradient vector and a directional scattering signal. Here, we present a process for fabricating the key optical elements required for this technique: phase and absorption gratings with periods of few micrometers and high aspect ratios, with a particular focus on two dimensional grating structures. The fabrication process is based on deep reactive ion etching in silicon and electroplating of gold.

Keywords: X-ray imaging, X-ray metrology, Phase contrast imaging, Grating interferometry, Deep reactive ion etching, Gold electroplating

1. Introduction

X-ray imaging is nowadays widely used in many applications such as medical diagnosis, industrial testing, and luggage inspection. Currently, these applications rely on X-ray attenuation as fundamental contrast mechanism. Although this works well in applications where strongly absorbing objects are to be imaged, much higher contrast can be obtained in low absorbing materials such as soft tissue by using phase-contrast imaging [1, 2, 3].

Grating interferometry was first introduced for differential phase contrast imaging at synchrotron sources [4, 5, 6], measuring the refraction angle in the direction perpendicular to the lines of the two line gratings. Its range of possible applications has been extended considerably by introducing a third grating, which enables implementing this method at conventional X-ray tube sources [7, 8, 9]. Due to its high sensitivity to refraction angles, grating interferometry has also found application in the field of X-ray mirror metrology [10, 11, 12]. More recently, it has also been used to explore the wavefront and properties of a hard X-ray free electron laser [13]. In addition to the refraction angle, grating interferometry also provides a dark-field signal, which is related to small-angle scattering in the sample [14]. The technique has also been used for lateral coherence measurements [11, 15].

More recently, grating interferometry has been extended to simultaneously measure the differential phase in two perpendicular directions, which can lead to an improved reconstruction of the wavefront phase. Two-dimensional grating interferometry, which uses gratings structured in two dimensions rather than line gratings, has been used for phase and directional dark-field imaging [16, 17, 18] as well as for X-ray lens metrology [19].

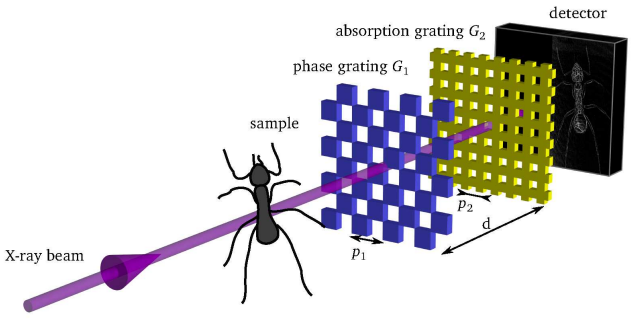

Figure 1: Setup sketch for imaging using a 2D grating interferometer, consisting of a checkerboard patterned beam splitter grating G_1 and a mesh-patterned analyzer grating G_2. For plane-wave illumination, the intergrating distance d is chosen to be one of the distances D_n (Eq. 1) where high interference pattern contrast is observed.

Existing fabrication processes for one-dimensional line gratings are based on anisotropic wet etching of silicon substrates of (110) crystal orientation [20] or X-ray lithography in thick layers of photoresist [21, 22]. Here, we present a fluoride based deep reactive ion etching (DRIE) process that not only enables the fabrication of high aspect ratio one-dimensional gratings, but can equally well be applied to the fabrication of two-dimensional structures.

A two-dimensional grating interferometry setup is sketched in Fig. 1. The X-ray beam, emitted from an X-ray source of sufficient brightness such as a synchrotron, impinges on and interacts with a sample which is to be imaged. Downstream of the sample, a π phase shifting transmission grat-

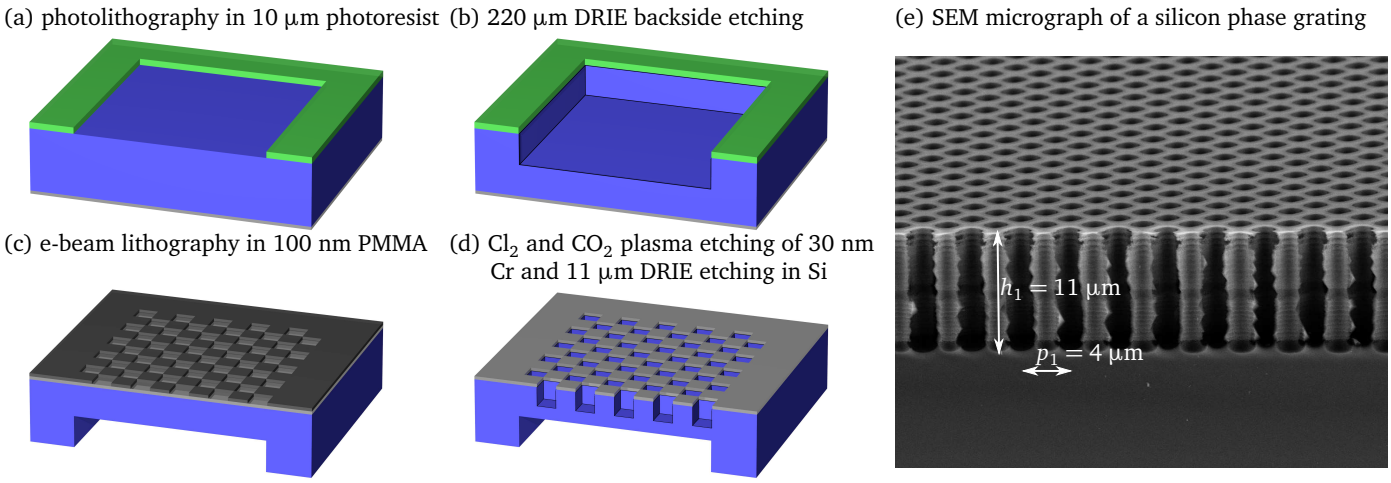

Figure 2: Phase grating fabrication process. (a – b) Backside etching to reduce absorption in the silicon substrate. (c – d) E-beam lithography and etching of the checkerboard grating pattern. (e) Cross-section of a silicon phase grating of period $p_1 = 4$ µm and structure height providing π phase shift at a photon energy of 9 keV.

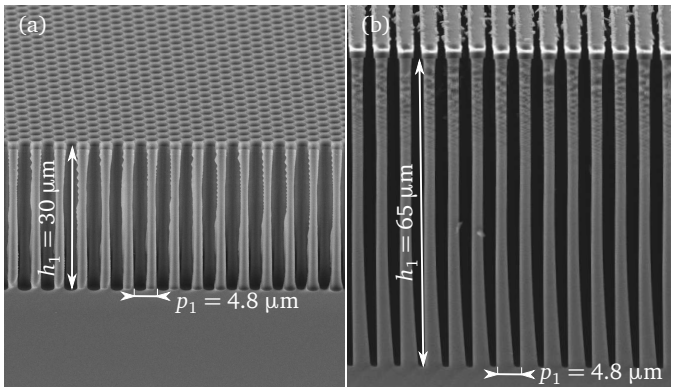

Figure 3: High aspect ratio phase gratings, fabricated using photolithography and deep reactive ion etching. (a) Checkerboard pattern phase grating for π phase shift at a photon energy of 23 keV. (b) One-dimensional line phase grating for π phase shift at 50 keV photon energy.

ing diffracts the incident radiation mainly into a plus and a minus first diffraction order. In a two-dimensional interferometer, the checkerboard patterned phase grating simultaneously diffracts the radiation in the vertical and the horizontal direction [23]. These diffracted waves interfere downstream, producing a mesh-shaped intensity modulation [24]. For plane-wave illumination, these intensity modulations are located at distances

$$D_n = np_1^2/(8\lambda) \quad (1)$$

from the phase grating, where n is an odd number, p_1 is the phase grating period and λ the wavelength of the radiation.

Any refraction of the incident radiation by the sample leads to a locally modified propagation direction of the X-ray beam and of the diffracted waves downstream of the phase grating. As a consequence, a shift of the interference pattern is observed, which is proportional to the refraction angle in the sample. Simultaneously, the contrast of the interference pattern is decreased if the features in the sample that are smaller than the camera resolution are scattering the radiation, which produces a dark-field signal [14]. Typically, the camera resolution is not sufficient to resolve the interference pattern, which has a period on the order of few µm. An analysis is nevertheless possible, by superimposing the interference pattern with a mesh-shaped absorbing analyzer grating G_2 of same period as the interference pattern. The interference pattern can either be analyzed by a phase stepping approach, shifting one of the gratings in multiple steps over a grating period as described in [16], or by using a moiré fringe analysis approach [17]. Both methods allow Fourier analysis to extract the local interference pattern shift, as well as changes in the pattern contrast. Using two-dimensional gratings, these quantities can be determined in the horizontal and the vertical direction simultaneously.

The key optical elements for grating interferometry are the diffraction gratings, with their micrometer-sized structures and high aspect ratios, whose fabrication we will describe in the following.

2. Grating fabrication

The requirements on the phase grating structures G_1 are driven by the demand for a short grating interferometer setup and high efficiency at the X-ray photon energies used. Reasonable inter-grating distances d on the order of less than half a meter (Fig. 1) are obtained for phase grating periods on the order of few µm (Eq. 1). Simultaneously, the grating structure should phase shift the X-ray wave by π (i.e. by half a wavelength).

In the process described here, the phase shifting is achieved with silicon structures. The required phase shift of π is attained with a structure height of 11 µm height for 9 keV photon energy. For higher photon energies, which have a higher penetration depth and can thus be used to image thicker objects, proportionally larger grating heights are required, such as 65 µm at 50 keV photon energy.

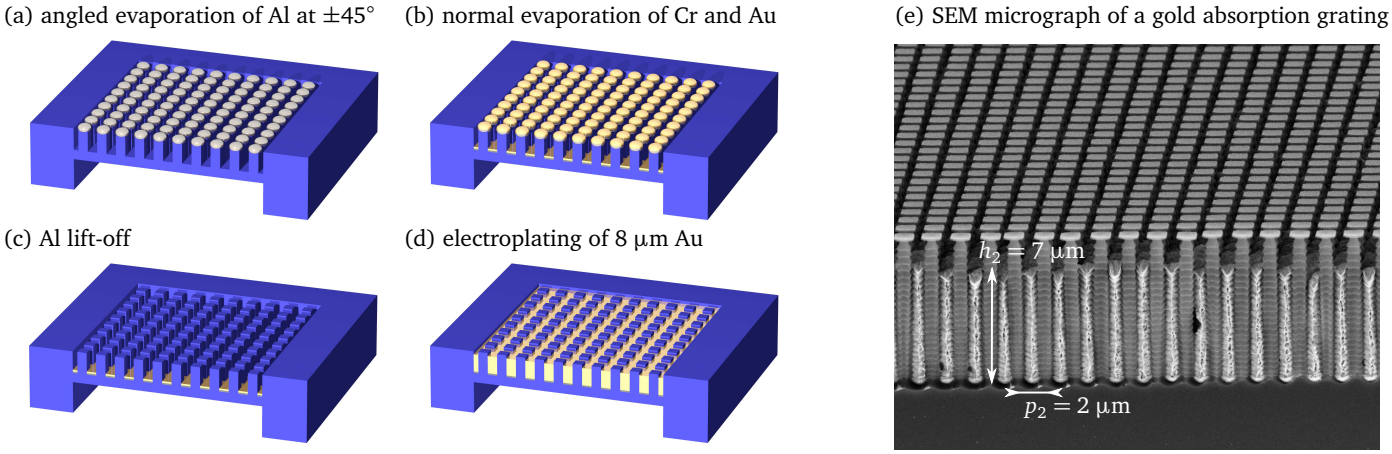

Figure 4: Absorption grating fabrication process. (a) Starting with a mesh-patterned grating fabricated as described in Fig. 2, a sacrificial Al layer is evaporated on the top of the grating structures. (b) Normal incidence evaporation of the Cr and Au plating base. (c) Aluminium etching and lift-off. (d) Electroplating of gold. (e) Cross-section of a gold absorption grating of period $p_2 = 2$ µm and structure height sufficient to absorb 90% of the incident intensity at a photon energy of 9 keV.

At low photon energies, the absorption of the bulk silicon substrate is considerable. At 9 keV, a 250 µm thick silicon wafer absorbs more than 90% of the incident intensity. To reduce absorption, the silicon substrate has to be thinned locally. All the fabrication steps described in the following were performed in a class 100 cleanroom environment. The thinning is achieved by spin coating the polished backside of the 100 mm diameter silicon wafer of (100) crystal orientation with a 10 µm thick layer of photoresist (Rohm and Haas Megaposit SPR220-7.0, spin coated with an acceleration of 300 rpm/s to a speed of 2000 rpm for 45 seconds). After photolithography (90 seconds exposure at 18 mW on the g-Line) followed by a 90 second backe at 115° on a hotplate and development (60 seconds in Rohm and Haas Megaposit MF24a) [Fig. 2(a)], the wafer backside is etched to a depth of about 220 µm using a deep reactive ion etching process [Fig. 2(b)]. The etch process consists of five hundred alternating etch and passivation steps in an inductively coupled plasma etching system (Oxford PlasmaLab System100), using SF_6 as etch gas and C_4F_8 for sidewall passivation. After the etching, the photoresist can be removed in *N*-Methyl-2-pyrrolidon (NMP) or by oxygen plasma ashing.

For small area gratings, the frontside of the wafer was then coated by a 30 nm thick layer of thermally evaporated chromium and a 100 nm thick layer of poly(methyl methacrylate) (PMMA, 600k molecular weight, 2% in chlorobenzene solution) by spin-coating with an acceleration of 300 rpm/s to a speed of 2000 rpm for 45 seconds, followed by a bake at 170° for 60 seconds on a hotplate. The checkerboard grating pattern with a grating period of 4 µm [Fig. 2(c)] was written by an electron beam writer system (Leica LION LV-1, 2.5 keV electron energy) in continuous-path writing mode, using a defocus of 24 µm and a line dose of 1 nC/cm to control the line width [25]. The checkerboard pattern was written by exposing two orthogonal gratings with diagonal lines, where the critical area dose is attained only at the intersection of two exposed lines. Compared to independently exposing each square of the checkerboard, this approach reduces the number of elements and thereby considerably decreases the writing time. The continuous-path writing enables producing large area gratings without introducing field stitching errors [26]. Grating structures fabricated for infrared coupling and filtering have been shown to have an accuracy of the average period in the sub-nanometer range [27, 28]. This high level of placement accuracy is essential for highly accurate grating-interferometry based wavefront metrology with an angular sensitivity on the order of 10 nrad, as described in detail elsewhere [13].

After spray-development (isopropanol and methyl isobutyl ketone (MIBK), 1:1 for 30 seconds), the PMMA pattern is transferred into the chromium hard mask by a plasma etching process using Cl_2 and CO_2 as reactive gases [Fig. 2(d)]. The grating structures are etched to a depth of 11 µm in a deep reactive ion etching process, consisting of 25 alternating etch and passivation steps (using SF_6 as reactive etch gas and C_4F_8 for sidewall passivation in an Oxford PlasmaLab System100). The chromium etch mask can then be removed, either by using plasma etching or using chromium wet etching. An SEM micrograph of a resulting checkerboard type phase grating is shown in Fig. 2(e).

For large area gratings, the chromium hard mask, PMMA and e-beam patterning were replaced by SPR220 photoresist and photolithography. This approach is favorable as it allows pattering of full 100 mm wafer sized gratings without being constrained by the pattering speed of the electron beam writer. The resist was deposited, exposed and developed as described previously for the backside patterning and etching. Two examples of high-aspect ratio gratings fabricated using this method are shown in Fig. 3.

The interference pattern produced by a checkerboard type phase grating is best analyzed by a highly absorbing mesh-shaped analyzer grating. Highly absorbing materials in the X-ray range are materials of high atomic number Z and in consequence high density, for example gold, iridium or plat-

inum. Of these, gold is the most widely used material in microfabrication with a wide range of applications in electrical connectors and printed circuit boards, where it is used due to its good electrical conductivity and its corrosion-resistance, which is why many electroplating baths are commercially available.

Our fabrication process for gold gratings is based on a silicon mold, that is fabricated in the same manner as the phase gratings G_1 (Fig. 2). The only difference is that the grating pattern is mesh-shaped and has a smaller grating period of only $p_2 = 2$ μm. For an X-ray photon energy of 9 keV, a gold structure height of 7 μm absorbs almost 90% of the incident intensity - largely sufficient for good contrast.

Following the silicon mold fabrication, a sacrificial layer of 2×300 nm aluminium is thermally evaporated at 45° incidence angle with respect to the surface, in a process inspired by Ref. [20]. The goal is to deposit aluminium only on the top of the silicon pillar array and not into the grooves [Fig. 4(a)]. In order to achieve this in a mask-less process, the evaporation direction is chosen to be almost diagonal with respect to the mesh grating structures. A large quantity of aluminium is evaporated in order to provide some shadowing of the sidewalls and ensure that the later orthogonal evaporation steps only cover the groove bottom.

In subsequent evaporation steps, this time perfectly orthogonal to the chip surface, a 20 nm chromium adhesion layer and a 30 nm gold plating base are thermally evaporated [Fig. 4(b)]. By etching away the aluminium in a solution of nitric- and phosphoric acid, the chromium and gold deposited on the top of the silicon pillars are lift off, leaving a conducting gold plating base only at the trench bottom [Fig. 4(c)]. The silicon mold is then filled with gold by electroplating [Fig. 4(d)], using a current density of 1 mA/cm^2 in a commercially available gold plating solution (Autronex CC-AF-B by Enthone). An SEM micrograph of a mesh patterned absorbing analyzer grating is shown in Fig. 4(e).

For high photon energies, increasing the structure height is desirable in order to maintain good X-ray contrast. At a photon energy of 60 keV for instance, 100 μm high gold grating structures transmit over 40% of the incident intensity. Residual transmission directly impacts the visibility of the phase stepping signal, which inversely proportional to the noise in the resulting image [29]. In practice the structure height is limited by the difficulty of evaporating a plating base only on the trench bottom and not on the sidewalls of large area gratings with high aspect ratio, and by the stability of the silicon pillars. The second problem can be reduced by using a stack of two one-dimensional gratings with orthogonal line orientation, at the cost of a more complex experimental setup and increased undesired absorption in the additional grating substrates.

As an alternative approach to absorbing analyzer gratings, one can envision fabricating a mesh-shaped silicon grating filled with scintillator material [30, 31]. This arrangement can provide superior contrast, as the residual transmission is not recorded by the camera, which observes only the visible light produced by the scintillator material. Such a grating would be the two-dimensional equivalent to the one-dimensional structured scintillator grating as described elsewhere [32, 33].

3. Imaging results

Two dimensional grating interferometry can be used both for differential phase-contrast imaging and for dark-field imaging [16]. An exemplary dark-field image of an ant is on display in Fig. 5.

The directional dark field image reveals information on the orientation of features that are much smaller than the image resolution and scatter the X-rays. This dataset has been recorded at the beamline ID19 of the European Synchrotron Radiation Facility [35]. A photon energy of 23 keV was selected using a silicon (111) double crystal monochromator, and a two-dimensional checkerboard type phase grating of period $p_1 = 4.785$ μm, such as the one shown in Fig. 3(a), was placed at 150 m distance from the source. A two-dimensional gold absorption grating of period $p_2 = 2.400$ μm was placed $d = 479$ mm downstream of the phase grating G_1. The gold grating used in this experiment had been fabricated by using X-ray lithography [22] to pattern two one-dimensional gratings with orthogonal orientation, fabricated on both sides of the same substrate. The images were recorded using a powder scintillator and a lens-coupled charge coupled device (ESRF FReLoN) with an effective pixel size of 8 μm. A phase stepping signal in 8×8 phase steps over two grating periods was recorded and analyzed as described elsewhere [16].

4. Conclusions

We have presented a fabrication process that is suitable for producing two-dimensional gratings with large area and high aspect ratio. The process is based on e-beam or optical lithography, deep reactive ion etching into silicon and electroplating of gold. These two-dimensional grating structures are of use in X-ray grating interferometry, which is a highly successful phase- and dark-field imaging technique. Its recent extension to two dimensions, measuring the differential wavefront phase in two perpendicular direction simultaneously, can provide improved quality phase reconstructions, as well as a directional dark field signal.

Acknowledgements

T. W. acknowledges support from the French research networks (RTRA) "Digiteo" and "Triangle de la Physique" (grants 2009-034T and 2009-79D). This work was partly carried out with the support of the Karlsruhe Nano Micro Facility (KNMF), a Helmholtz Research Infrastructure at Karlsruhe Institute of Technology (KIT).

[1] R. Fitzgerald, Phys. Today 53(7) (2000) 23.
[2] A. Momose, Jpn. J. Appl. Phys. 44 (2005) 6355–6367.

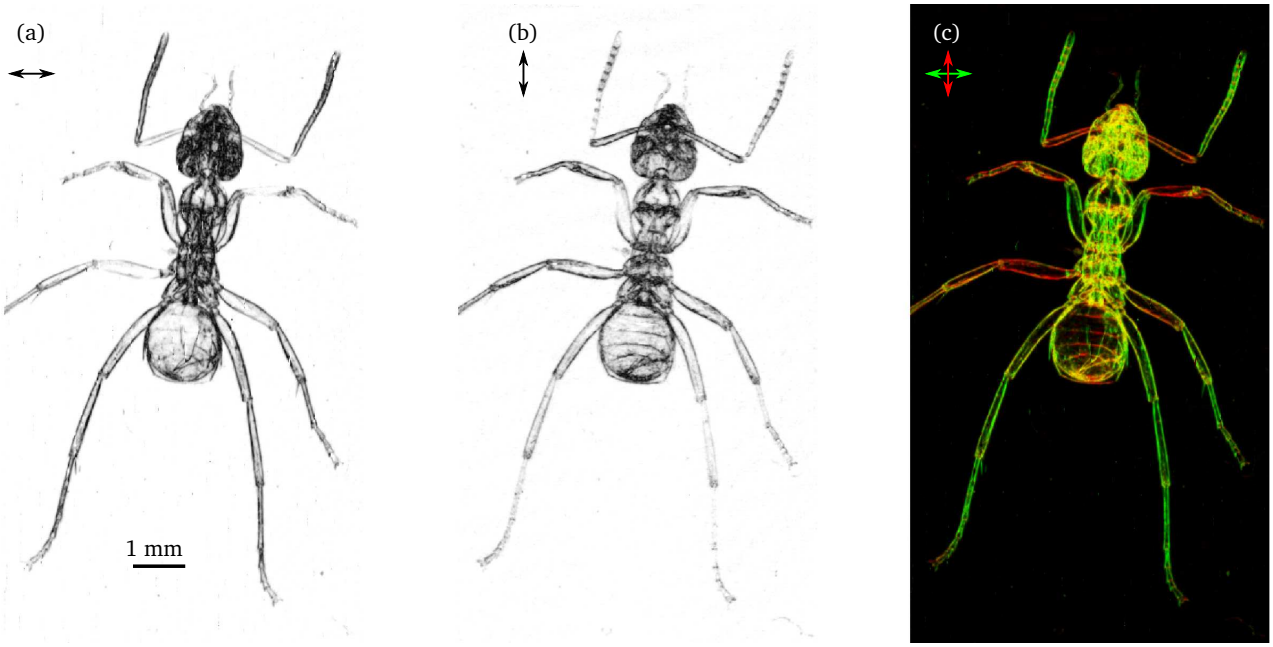

Figure 5: Directional dark field image of an ant. The directional scattering signal visualizes the orientation of the fine inner structure. (a) Horizontal scattering signal. (b) Vertical scattering signal, note the horizontally oriented structures in the antennae. (c) Color-coded scattering image. The green color channel depicts horizontal scattering, and the red one red vertical scattering. Isotropic scattering in both directions produces a yellow color. An image of the same ant is shown as parts of the ESRF Highlights 2011 [34].

[3] M. Bech, T. H. Jensen, O. Bunk, T. Donath, C. David, T. Weitkamp, G. L. Duc, A. Bravin, P. Cloetens, F. Pfeiffer, Z. Med. Phys. 20(1) (2010) 7–16.

[4] C. David, B. Nöhammer, H. Solak, and E. Ziegler, Appl. Phys. Lett. 81 (2002) 3287–3289.

[5] A. Momose, S. Kawamoto, I. Koyama, Y. Hamaishi, K. Takai, Y. Suzuki, Jpn. J. Appl. Phys. 42 (2003) 866–868.

[6] T. Weitkamp, A. Diaz, C. David, F. Pfeiffer, M. Stampanoni, P. Cloetens, E. Ziegler, OPt. Express 13 (2005) 6296–6304.

[7] F. Pfeiffer, T. Weitkamp, O. Bunk, C. David, Nat. Phys. 2 (2006) 258–261.

[8] T. Donath, F. Pfeiffer, O. Bunk, C. Grünzweig, E. Hempel, S. Popescu, P. Vock, C. David, Invest. Radiol. 45 (2010) 445-452.

[9] M. Stampanoni, Z. Wang, T. Thüring, C. David, E. Roessl, M. Trippel, R. A. Kubik-Huch, G. Singer, M. K. Hohl, N. Hauser, Invest. Radiol. 46 (2011) 801–806.

[10] T. Weitkamp, B. Nöhammer, A. Diaz, C. David, E. Ziegler, Appl. Phys. Lett. 86 (2005) 054101.

[11] A. Diaz, C. Mocuta, J. Strangl, M. Keplinger, T. Weitkamp, F. Pfeiffer, C. David, T. H. Metzger, G. Bauer, J. Synchrotron Radiat. 17 (2010) 299–307.

[12] H. Wang, K. Sawhney, S. Berujon, E. Ziegler, S. Rutishauser, C. David, Opt. Express 19 (2011) 16550-16559.

[13] S. Rutishauser, L. Samoylova, J. Krzywinski, O. Bunk, J. Grünert, H. Sinn, M. Cammarata, D.M. Fritz, C. David, Nat. Commun. 3 (2012) 947.

[14] F. Pfeiffer, M. Bech, O. Bunk, P. Kraft, E.F. Eikenberry, Ch. Brönnimann, C. Grünzweig, C. David, Nat. Mater. 7 (2008) 134–137.

[15] F. Pfeiffer, O. Bunk, C. Schulze-Briese, A. Diaz, T. Weitkamp, C. David, J. F. van der Veen, I. Vartanyants, I. K. Robinson, Phys. Rev. Lett. 94 (2005) 164801.

[16] I. Zanette, T. Weitkamp, T. Donath, S. Rutishauser, C. David, Phys. Rev. Lett. 105 (2010) 248102.

[17] H. Itoh, K. Nagai, G. Sato, K. Yamaguchi, T. Nakamura, T. Kondoh, C. Ouchi, T. Teshima, Y. Setomoto, T. Den, Opt. Express 19 (2011) 3339-3346.

[18] S. Berujon, H. Wang, I. Pape, K. Sawhney, S. Rutishauser, C. David, Opt. Lett. 37 (2012) 1622–1624.

[19] S. Rutishauser, I. Zanette, T. Weitkamp, T. Donath, C. David, Appl. Phys. Lett. 99 (2011) 221104.

[20] C. David, J. Bruder, T. Rohbeck, C. Grünzweig, C. Kottler, A. Diaz, O. Bunk, F. Pfeiffer, Microelectro. Eng. 84 (2007) 1172–1177.

[21] M. Matsumoto, K. Takiguchi, M. Tanaka Y. Hunabiki, H. Takeda, A. Momose, Y. Utsumi, T. Hattori, Microsyst. Technol. 13 (2007) 543–546.

[22] E. Reznikova, J. Mohr, M. Boerner, V. Nazmov, P.-J. Jakobs, Microsyst. Technol. 14 (2008) 1683–1688.

[23] J. Primot, N. Guérineau, Appl. Opt. 39 (2000) 5715–5720.

[24] I. Zanette, C. David, S. Rutishauser, T. Weitkamp, AIP Conf. Proc. 1221 (2010) 73–79.

[25] C. David, D. Hambach, Microelectron. Eng. 46 (1999) 219–222.

[26] B. Schnabel, E. B. Kley, Microelectron. Eng. 57–58 (2001) 327–333.

[27] C. David, D. Wiesmann, R. Germann, F. Horst, B.J. Offrein, R. Beyeler, H.W.M. Salemink, G.L. Bona, Microelectron. Eng. 57–58 (2001) 713–719.

[28] D. Wiesmann, R. Germann, G.L. Bona, C. David, D. Erni, H. Jäckel, J. Opt. Soc. Am. B 20 (2003) 417–423.

[29] K. Engel, D. Geller, T. Köhler, G. Martens, S. Schusser, G. Vogtmeier, E. Rössl, Nucl. Instrum. Methods Phys. Res. A 648 (2011) 202–207.

[30] P. Kleimann, J. Linnros, C. Fröjdh, C.S. Peterson, Nucl. Instrum. Methods Phys. Res. A 460 (2001) 15–19.

[31] A. Sahlholm, O. Svenonius, S. Petersson, Nucl. Instrum. Methods Phys. Res. A 648 (2011) S16–S19.

[32] S. Rutishauser, I. Zanette, T. Donath, A. Sahlholm, J. Linnros, C. David, Appl. Phys. Lett. 98 (2011) 171107.

[33] L. Yao-Hu, L. Xin, G. Jin-Chuan, Z. Zhi-Gang, N. Han-Ben, Chin. Phys. B 20 (2011) 042901.

[34] I. Zanette, T. Weitkamp, T. Donath, S. Rutishauser, C. David, ESRF Highlights (2011) 116–117.

[35] T. Weitkamp, P. Tafforeau, E. Boller, P. Cloetens, J.-P. Valade, P. Bernard, F. Peyrin, W. Ludwig, L. Helfen, J. Baruchel, AIP Conf. Proc. 1221 (2010) 33–38.